



Comprehensive Analysis of the Cycle Slip Detection Threshold in Kinematic PPP During Geomagnetic Storms

Qiang Li¹, Xing Su¹ (✉), Chunyan Tao², Junli Zhang³, Zhimin Liu¹, Jianhui Cui¹, Zeyv Ma¹, Baopeng Xu¹, and Yan Xu¹

¹ Shandong University of Science and Technology, Qingdao 266590, China
suxing@sdust.edu.cn

² Beijing Satellite Navigation Center, Beijing 100094, China

³ 32039 Troops, Beijing 100094, China

Abstract. Space weather events may affect the magnetosphere and ionosphere, and thus reduce the positioning capacity of global navigation satellite systems. The paper analyzes the BDS/GPS kinematic Precise Point Positioning (PPP) accuracy during the November 2021 geomagnetic storm to investigate the impact of the cycle slip (CS) detection on positioning accuracy under an active ionosphere. The results show that when using the conventional constant threshold of geometry-free (GF) CS detection, several stations in high latitudes present obvious accuracy anomalies and the maximum positioning error reaches 6 m. It is also found that the CS incidence increases significantly during the period of accuracy anomalies. When using the adaptive GF threshold, the kinematic PPP positioning accuracy and CS incidence return to the normal level, which proves that the underprivilege of conventional GF threshold that the geomagnetic storm could generate CS misjudgments and lead to an abnormal positioning accuracy. The average 3D positioning accuracies of 40 stations worldwide located at different latitudes show that the adaptive GF threshold could improve the average positioning accuracy of stations in high latitudes by 42.5%.

Keywords: Kinematic Precise Point Positioning · Geomagnetic Storm · Cycle Slip Detection · Adaptive Threshold

1 Introduction

The development of global navigation satellite systems plays an increasingly important role in various fields [1–5]. Autonomous navigation of constellations is a new mode of operation and control, which is a supplement and improvement to the existing mode of operation and control mainly based on ground-based control stations [6–10]. In autonomous navigation and intelligent operation, the influence of the space environment is a factor that should be considered.

Space weather events with short time scale variations such as flares and coronal mass ejections caused by solar activity can affect and harm the Earth's magnetosphere,

ionosphere, and middle and upper atmosphere. The ionosphere, an important component of near-Earth space, contains a large number of free electrons and positively charged ions that have a large impact on global navigation satellite systems [11–13]. During geomagnetic storms, huge amounts of energy are injected into the upper atmosphere in the form of enhanced electric fields, and energetic particles. This is accompanied by a complex response of the ionosphere and thermosphere to geomagnetic storms through the propagation of energy-momentum and thermosphere-ionosphere coupling [14]. Due to the prevalent thermosphere-ionosphere coupling process, perturbations in the thermosphere may affect the behavior of the ionosphere (including positive and negative ionospheric responses) during geomagnetic storms through wind field transport and compositional changes [15, 16].

The disturbance of the ionosphere by geomagnetic storms can lead to a significant impact on positioning performance [17, 18]. Alcay et al. [19] and Poniatowski et al. [20] studied several geomagnetic storms and found that the error of the kinematic precise point positioning (PPP) increases significantly during geomagnetic storms, and the degree of accuracy loss is related to the intensity of Total Electron Content (TEC) fluctuations.

In PPP, cycle slip (CS) detection is an important task [21–23]. Many methods have been proposed for CS detection, including Melbourne-Wübbena (MW) observations, geometry-free (GF) phase combination method, polynomial fitting method, Kalman filtering method, etc. [24]. Different methods are suitable for different situations, for instance, MW observations cannot detect the same CSs at dual frequency observations, the polynomial fitting method is suitable for detecting large CSs, and the geometry-free phase combination method suffers from ionospheric system bias, etc. [25]. The ionospheric perturbation is large during geomagnetic storms, and the geometry-free phase combination method may suffer from CS misclassification under low sampling rate conditions [26, 27].

The global kinematic positioning accuracy during the November 2021 geomagnetic storm is analyzed to investigate the influence of the GF CS detection threshold on positioning accuracy. The geomagnetic storm is a strong geomagnetic storm (the minimum Dst is less than -100 nT), and the BDS/GPS combined system is used in the experiment to improve the positioning robustness. The paper is organized as follows: Sect. 2 introduces the commonly used CS detection methods and the existing GF threshold model; Sect. 3 analyzes the space weather indicators during the geomagnetic storm; Sect. 4 details data processing strategies; In Sect. 5, we analyze the experimental results; Finally, the conclusion is given in Sect. 6.

2 Theory and Methods

2.1 TurboEdit Cycle Slip Detection Method

The current widely used method for CS detection in GNSS data processing is the TurboEdit method [28], which has the advantage of single station detection, a high success rate, and is suitable for CS detection of non-differential data. The TurboEdit method uses MW combination observable and GF combination observable for CS detection.

The MW combined observable equation is as follows [29, 30].

$$\varphi_{\Delta}\lambda_{\Delta} - \frac{f_1P_1 + f_2P_2}{f_1 + f_2} + N_{\Delta}\lambda_{\Delta} = 0 \quad (1)$$

where φ_{Δ} , λ_{Δ} represent the wide lane observable and their wavelengths, f_1, f_2 represent the frequencies of the two signals, P_1, P_2 represent the pseudo-range observable of the two signals, and N_{Δ} represent the ambiguity of the wide aisle observable. The ambiguity of the wide lane observable is used as the CS detection:

$$N_{\Delta} = \varphi_{\Delta} - \frac{f_1P_1 - f_2P_2}{\lambda_{\Delta}(f_1 + f_2)} \quad (2)$$

MW observable eliminates ionospheric errors, satellite and receiver clock differences, and satellite-station geometric distances. It is only affected by measurement noise and multipath errors. However, it cannot detect equaled CSs on two signals, therefore the phase GF combined observable is used as the CS detection quantity to continue the detection, and the GF phase observable is

$$L_{GF} = \lambda_1\varphi_1 - \lambda_2\varphi_2 = I/f_1^2 - I/f_2^2 + \lambda_1N_1 - \lambda_2N_2 + \varepsilon_{GF} \quad (3)$$

where, $I/f_1^2, I/f_2^2$ represent the ionospheric delay at two frequencies, and ε_{GF} represent the combined observation noise. The GF observable eliminates the effects of receiver clock difference, satellite clock difference, and tropospheric delay. It contains only ionospheric errors and frequency-dependent measurement noise, therefore it is also sensitive to equaled CSs on two signals.

2.2 Adaptive GF Threshold Model

The difference between adjacent epochs is generally used for real-time CS detection. In practice, there is no uniform threshold for all cases, and the detection thresholds for MW and GF are usually set to 1–2 cycles and 5–15 cm to detect smaller CSs [31]. For instance, in the open-source package RTKLIB, the GF threshold is set to 5 cm by default [32]. The GF CS detection is highly accurate, and could detect small CSs when set to 5 cm, but for large sampling intervals or when the ionosphere is active, the threshold is slightly more stringent, and could easily lead to misclassification [33].

To reduce the misjudgment of CS caused by improper GF threshold setting, adaptive thresholds can be established using certain methods. The GF adaptive threshold models applicable to GPS and BDS satellites are introduced, respectively. Both models are developed by analyzing the characteristics of the difference of GF observations between adjacent epochs under different ionospheric conditions and considering the effects of data sampling interval and satellite elevation. For GPS satellites, the GF threshold model is as follows [33]:

$$T = l \times T_0 \quad (4)$$

where l is the weighting factor associated with the satellite elevation and is calculated as follows.

$$l = \begin{cases} 1, & e \geq E \\ \sqrt{\sin(E)/\sin(e)}, & e < E \end{cases} \quad (5)$$

where e denotes the satellite elevation of the current epoch; E denotes the critical satellite elevation, where the weighting factor takes effect when e is less than E , which is usually taken as 30° . Where T_0 is the empirical threshold value related to the data sampling interval R , calculated as follows.

$$T_0 = \begin{cases} 0.05, & 0 < R \leq 5 \text{ s} \\ 0.03 + 0.004 \times R, & 5 \text{ s} < R \leq 30 \text{ s} \\ 0.15, & 30 \text{ s} < R \leq 60 \text{ s} \end{cases} \quad (6)$$

For BDS satellites, a GF threshold model that takes into account the satellite elevation, data sampling interval, and satellite orbit type is as follows [34].

$$T = k \times T_0 \quad (7)$$

where T_0 is the empirical threshold related to the sampling interval R established using BDS observation data.

$$T_0 = \begin{cases} 5, & 0 < R \leq 8 \text{ s} \\ 0.51 \times R + 0.92, & 8 \text{ s} < R \leq 30 \text{ s} \\ 16.22, & 30 \text{ s} < R \leq 60 \text{ s} \end{cases} \quad (8)$$

k is a weighting factor that takes into account the satellite orbit type and elevation. For GEO satellites, k is 5; for IGSO/MEO satellites, k is the l calculated using Eq. (5).

3 Space Weather Indices Variations

To analyze the geomagnetic storm occurring on November 3, 2021, this paper uses space weather indices including the solar wind (SW) speed, the Bz component of the interplanetary magnetic field (IMF), and the Dst index. Figure 1 shows the variations in the above indices.

The Dst index is usually used as the basis for classifying each phase of a geomagnetic storm. The geomagnetic storm started at about 18:00 on November 3, when the solar wind speed began to soar and the storm sudden commencement (SSC) began to appear; and then entered the main phase of the storm at about 19:00, when the Dst index reached its peak and began to enter the declining phase, and the SW speed had reached about 650 km/s at that time; with the development of the main phase, the IMF Bz dropped and then there were 2 recoveries, the lowest reached -12.6 nT; the Dst index kept falling, the lowest reached -105 nT, and the SW speed remained at about 700 km/s throughout the main phase; after entering the recovery phase (November 4, 12:00), all indices began to gradually return to normal.

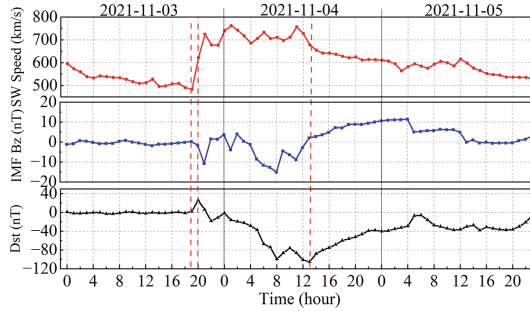


Fig. 1. Variations of space weather indices from November 3–5, 2021

4 Experimental Analysis

4.1 Data Processing Strategies

The geomagnetic storm lasted for several days. The paper focuses on analyzing the positioning accuracy of the initial and main phases of the geomagnetic storm, and we continuously process the observation data of 40 MGEX stations worldwide on November 3–4 to ensure that the positioning result has been initialized before the occurrence of the geomagnetic storm. WUM precision orbit and precision clock products are used. The conventional constant GF detection threshold (0.05 m) and the adaptive threshold model in Sect. 2.2 are used for data processing, respectively, and other data processing strategies are kept consistent. The solution mode is Kinematic, using dual-frequency ionosphere-free observations with a data sampling interval of 30 s and a satellite cutoff elevation taken as 10° .

4.2 Analysis of the Experiment Results

Since the geomagnetic storm affects each station at different periods and degrees, to show the variations in positioning accuracy during the geomagnetic storm in detail, the RMS value of positioning error of each station is counted in 15-min windows. Under normal conditions, thanks to high-precision satellite orbit and clock, PPP can reach static millimeter and kinematic centimeter to decimeter accuracy [35–41]. The positioning results show that a few stations show obvious accuracy anomalies, i.e., the positioning accuracy exceeds 1 m, during certain periods, as shown in Fig. 2. There are 6 stations with positioning errors exceeding 1 m during the study period, namely DAV1, GCGO, KIRU, NABG, NYA1, and SOD3, all of which are located at high latitudes. High-energy particles enter the middle and upper atmosphere along the geomagnetic lines of force at both levels of the Earth during the geomagnetic storm, and the ionosphere at high latitudes is the first to be affected by geomagnetic storms, therefore the positioning accuracy of stations at high latitudes is more likely to be abnormal.

The positioning errors in the E, N, and U directions and the CS incidence (the ratio of satellites with a CS to the total number of satellites) for each epoch are plotted in Fig. 3a. It can be seen that the CS incidence increases abnormally in some periods up to 90% for

the six stations in the figure, and the positioning error increases accordingly when the incidence of CSs increases. This is because the filter resets the ambiguity parameters of the corresponding satellites when a CS is detected, to avoid the fluctuation of positioning accuracy due to incorrect estimation of ambiguity. However, if there are a large number of misjudged CSs, the positioning accuracy will be abnormal due to the simultaneous resetting of more ambiguous parameters.

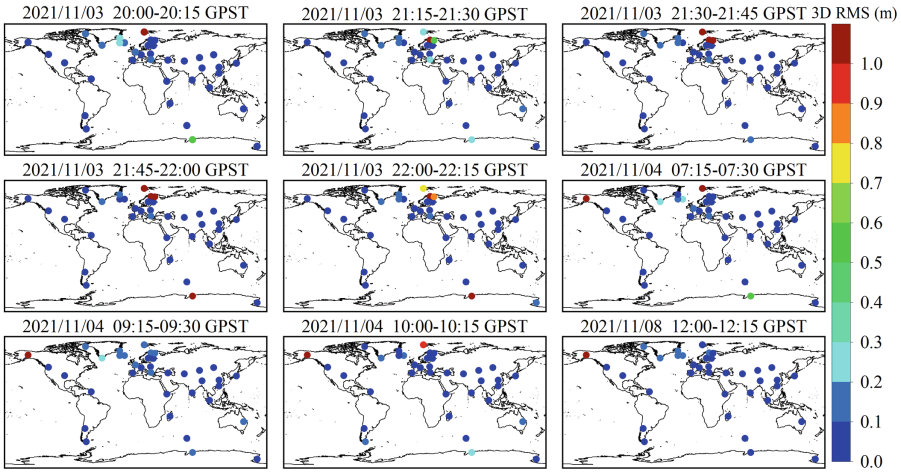


Fig. 2. 3D Kinematic positioning accuracy using the constant GF threshold for some periods on November 3–4, 2021.

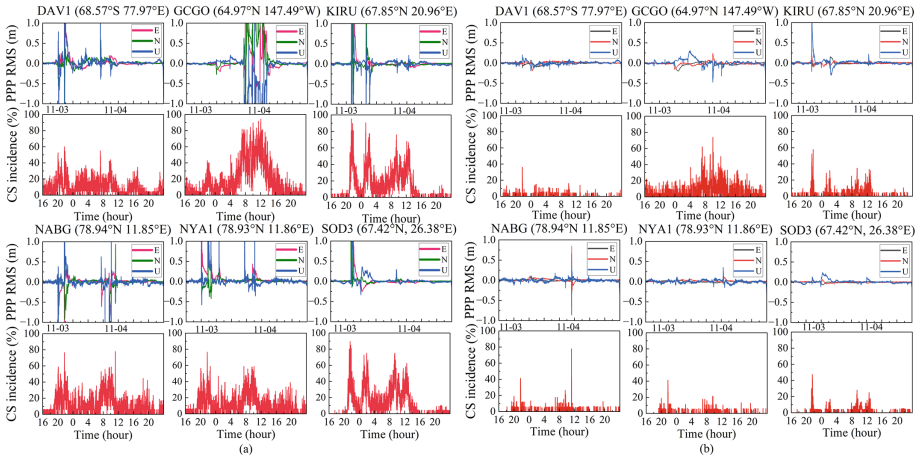


Fig. 3. Positioning error time series and the CS incidence: **a** the constant GF threshold; **b** the adaptive GF threshold.

The data are reprocessed using the adaptive GF threshold model. The positioning error time series and the CS incidence of the six stations after processing are plotted

in Fig. 3b. It can be seen that after implementing the adaptive GF threshold for CS detection, the overall CS incidence becomes smaller and smoother. For stations DAV1, GCGO, NYA1, and SOD3, the anomalous jump in the positioning error has completely disappeared; for KIRU and NABG, the CS misjudgment phenomenon has been significantly improved, with only 11 epochs of KIRU having a positioning error of more than 1 m and NABG having only one obvious CS misjudgment, and the corresponding positioning error does not exceed 0.9 m. From an overall perspective, the CS misjudgment phenomenon has been significantly improved for six stations.

The average positioning accuracy of all stations during the geomagnetic storm period (Nov. 3, 18:00–Nov. 5, 00:00) is calculated, and the average accuracy of different latitude areas was counted with 0–30° as low latitude, 30–60° as middle latitude, and above 60° as high latitude, and the results are shown in Table 1. It can be seen that the positioning accuracy of stations at high latitudes is improved by 42.5% when using adaptive thresholds for CS detection compared with constant thresholds; the accuracy of stations at middle and low latitudes does not change significantly because they are less affected by geomagnetic storms.

The 3D positioning accuracy of all the reprocessed stations is shown in Fig. 4. It can be seen that the 3D positioning accuracy of all stations in the selected period is less than 1 m. The positioning accuracy of the adaptive threshold is greatly improved compared to the constant GF threshold.

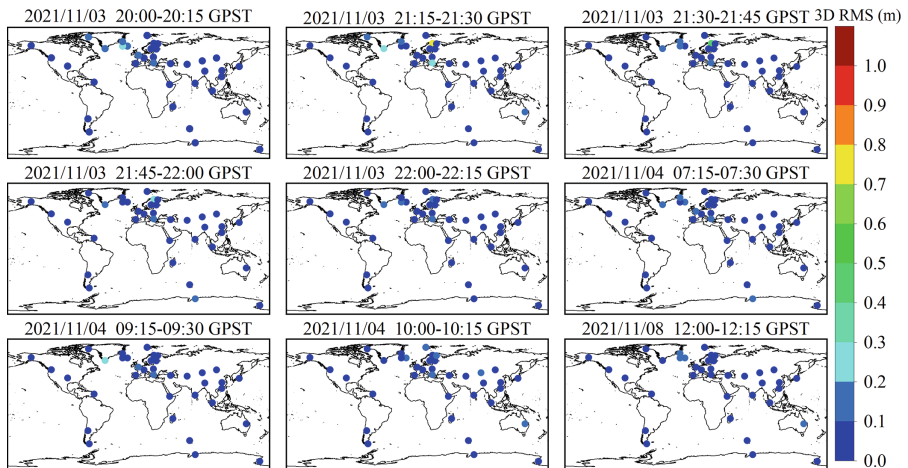


Fig. 4 3D Kinematic positioning accuracy using the adaptive GF threshold for some periods on November 3–4, 2021

Table 1. Average 3D positioning accuracies of stations in different latitudes (m)

Region	Constant GF threshold	Adaptive GF threshold	Improvement (%)
High latitudes	0.105	0.061	42.5
Mid-latitudes	0.056	0.052	7.9
Low latitudes	0.054	0.055	-2.3

5 Conclusion

The paper investigates the effect of GF threshold settings on the kinematic BDS/GPS PPP positioning accuracy during the November 2021 geomagnetic storm. The following conclusions are obtained from the experiment analysis:

- (1) During the geomagnetic storm, when the constant GF threshold of 0.05 m is used for CS detection, the CS incidence in some periods of several stations located at high latitudes increases abnormally, up to 90%, and the positioning accuracy in the corresponding periods decreases significantly, with the maximum positioning error exceeding 6 m. For real-time CS detection, the active ionosphere can cause drastic changes in the GF phase observations, and the use of general thresholds at this time will result in a large number of CS misjudgments. When the filter detects a CS, it will reset the ambiguity parameters of the corresponding satellite, and when there are multiple satellite misjudgments, the ambiguity parameters are reset in large numbers, which leads to significant degradation of positioning accuracy.
- (2) Kinematic PPP experiments using the adaptive GF threshold model show that the CS incidence in the above six stations returns to normal, and the positioning accuracy is within 1 m. Compared with the conventional constant threshold, the adaptive threshold can significantly reduce CS misjudgment and restore the positioning accuracy to the normal level.
- (3) The average 3D positioning accuracies in different latitudes show that the adaptive threshold model shows superiority under the geomagnetic storm condition, and it can improve the average positioning accuracy of stations in high latitudes by 42.5%.

Acknowledgments. The work was supported by the National Natural Science Foundation of China (No. 42304036); Shandong Provincial Natural Science Foundation, China (Grant number ZR2023MD054, ZR2021QD131); Key Laboratory of Geomatics and Digital Technology of Shandong Province; and Scientific Research Foundation of Shandong University of Science and Technology for Recruited Talents (Grant number 2017RCJJ072).

References

1. Li M et al (2015) Assessment of precipitable water vapor derived from ground-based BeiDou observations with precise point positioning approach. *Adv Space Res* 55(1):150–162

2. Geng T, Xie X, Fang R, Su X, Zhao Q, Liu G, Li H, Shi C, Liu J (2016) Real-time capture of seismic waves using high-rate multi-GNSS observations: application to the 2015 M_w 7.8 Nepal earthquake. *Geophys Res Lett* 43(1):161–167
3. Su X, Geng T, Li W, Zhao Q, Xie X (2017) Chang'E-5T orbit determination using onboard GPS observations. *Sensors* 17(6):1260
4. Geng T, Su X, Zhao Q (2012) MEO and HEO satellites orbit determination based on GNSS onboard receiver. In: China Satellite Navigation Conference (CSNC) 2012 proceedings. Springer, Berlin, Heidelberg, pp 223–234
5. Ma H, Verhagen S, Psychas D, Monico JFG, Marques HA (2021) Flight-test evaluation of integer ambiguity resolution enabled PPP. *J Surv Eng* 147(3):04021013
6. Song X, Mao Y (2021) Autonomous navigation principles and methods for BeiDou navigation satellite system, 1st edn. National Defense Industry Press, Beijing
7. Guo J, Zhao Q, Geng T, Su X, Liu J (2013) Precise orbit determination for COMPASS IGS0 satellites during yaw maneuvers. In: China Satellite Navigation Conference (CSNC) 2013 proceedings. Springer, Berlin, Heidelberg, pp 41–53
8. Su M, Zhao Q, Guo J, Su X, Hu Z, Guo H (2018) Phase center calibration for receiver antenna and its impact on precise orbit determination of BDS satellites. *Acta Geodaetica et Cartographica Sinica* 47(S0):78–85
9. Su X, Geng T, Zhao Q, Qu L, Li X (2012) Research on integrated orbit determination combined satellite-ground and inter-satellite observation based on Helmert method of variance components estimate. In: China Satellite Navigation Conference (CSNC) 2012 proceedings. Springer, Berlin, Heidelberg, pp 349–359
10. Ma H, Zhao Q, Verhagen S, Psychas D, Liu X (2020) Assessing the performance of multi-GNSS PPP-RTK in the local area. *Remote Sens* 12(20):3343
11. Fang T, Kubaryk A, Goldstein D, Li Z, Fuller-Rowell T, Millward G, Singer HJ, Steenburgh R, Westerman S, Babcock E (2022) Space weather environment during the SpaceX Starlink satellite loss in February 2022. *Space Weather* 20(11):e2022SW003193
12. Klobuchar J (1987) Ionospheric time-delay algorithm for single-frequency GPS users. *IEEE Trans Aerosp Electron Syst* AES-23(3):325–331
13. Li Q, Su X, Xie X, Tao C, Cui J, Chen H, Liu Z (2022) Accuracy analysis of error compensation in the ionospheric model of BDS broadcasting based on ABC-BP Neural network. In: China Satellite Navigation Conference (CSNC) 2022 proceedings. Springer, Singapore, pp 54–63
14. Prolss GW (2011) Density perturbations in the upper atmosphere caused by the dissipation of solar wind energy. *Surv Geophys* 32(2):101–195
15. Aa E, Zhang S, Erickson PJ, Coster AJ, Goncharenko LP, Varney RH, Eastes R (2021) Salient midlatitude ionosphere-thermosphere disturbances associated With SAPS during a minor but geo-effective storm at deep solar minimum. *J Geophys Res: Space Phys* 126(07):e2021JA029509
16. Huang C (2019) Long-lasting penetration electric fields during geomagnetic storms: observations and mechanisms. *J Geophys Res Space Phys* 124(11):9640–9664
17. Tariku YA (2021) The geomagnetic storm time response of the mid latitude ionosphere during solar cycle 24. *Radio Science* 56(12):e2021RS007340
18. Li Q et al (2022) Performance analysis of GPS/BDS broadcast ionospheric models in standard point positioning during 2021 strong geomagnetic storms. *Remote Sens* 14(17):4424
19. Alcay S (2022) Ionospheric response to extreme events and its effects on precise point positioning. *Indian J Phys* 96(13):3721–3734
20. Poniowski M, Nykiel G (2020) Degradation of kinematic PPP of GNSS stations in central Europe caused by medium-scale traveling ionospheric disturbances during the St. Patrick's day 2015 geomagnetic storm. *Remote Sens* 12(21):3582
21. Li M, Qu L, Zhao Q, Guo J, Su X, Li X (2014) Precise point positioning with the BeiDou navigation satellite system. *Sensors* 14(01):927–943

22. Geng T, Su X, Fang R, Xie X, Zhao Q, Liu J (2016) BDS precise point positioning for seismic displacements monitoring: benefit from the high-rate satellite clock corrections. *Sensors* 16(12):2192
23. Qu L, Zhao Q, Li M, Guo J, Su X, Liu J (2013) Precise point positioning using combined Beidou and GPS observations. In: China Satellite Navigation Conference (CSNC) 2013 proceedings. Springer, Berlin Heidelberg, pp 241–252
24. Cai C, Liu Z, Xia P, Dai W (2012) Cycle slip detection and repair for undifferenced GPS observations under high ionospheric activity. *GPS Solutions* 17(2):247–260
25. Miao Y, Sun ZW, Wu SN (2011) Error Analysis and cycle-slip detection research on satellite-borne GPS observation. *J Aerosp Eng* 24(01):95–101
26. Chen L, Zhang L (2016) Cycle-slip processing under high ionospheric activity using GPS triple-frequency data. In: China Satellite Navigation Conference (CSNC) 2016 proceedings. Springer, Singapore, pp 411–423
27. Nie W, Rovira-Garcia A, Li M, Fang Z, Wang Y, Zheng D, Xu T (2022) The mechanism for GNSS-based kinematic positioning degradation at high-latitudes under the March 2015 great storm. *Space Weather* 20(06):e2022SW003132
28. Blewitt G (1990) An automatic editing algorithm for GPS data. *Geophys Res Lett* 17(3):199–202
29. Melbourne WG (1985) The case for ranging in GPS-based geodetic systems. In: Proceedings of the first international symposium on precise positioning with the global positioning system. American Geophysical Union, Maryland, pp 373–386
30. Wubben G (1985) Software developments for geodetic positioning with GPS using TI 4100 code and carrier measurements. In: Proceedings of the first international symposium on precise positioning with the global positioning system. American Geophysical Union, Maryland, pp 403–412
31. Zhang X, Guo F, Zhou P (2013) Improved precise point positioning in the presence of ionospheric scintillation. *GPS Solutions* 18(01):51–60
32. RTKLIB ver. 2.4.2 Manual. https://www.rtklib.com/prog/manual_2.4.2.pdf. Last Accessed 22 Nov 2022
33. Zhang X, Zeng Q, He J, Kang C (2017) Improving TurboEdit real-time cycle slip detection by the construction of threshold model. *Geomatics Inf Sci Wuhan Univ* 42(3):285–292
34. Ding Z, He K, Liu D, Li M, Zong Y (2022) BDS cycle slip detection method based on adaptive threshold model GF combination. *J Geodesy Geodyn* 42(7):734–739
35. Wang B, Lou Y, Liu J, Zhao Q, Su X (2015) Analysis of BDS satellite clocks in orbit. *GPS Solutions* 20(4):783–794
36. Chen H, Niu F, Su X, Geng T, Liu Z, Li Q (2021) Initial results of modeling and improvement of BDS-2/GPS broadcast ephemeris satellite orbit based on BP and PSO-BP neural networks. *Remote Sens* 13(23):4801
37. Ma H, Verhagen S (2020) Precise point positioning on the reliable detection of tropospheric model errors. *Sensors* 20(6):1634
38. Chen H, Su X, Niu F, Li Q, Liu Z (2022) BDS-2 broadcast ephemeris orbit error compensation based on ABC-BP neural network. In: China Satellite Navigation Conference (CSNC) 2022 proceedings. Springer, Singapore, pp 64–74
39. Su M, Su X, Zhao Q, Liu J (2019) BeiDou augmented navigation from low earth orbit satellites. *Sensors* 19(1):198
40. Su X, Chen H, Zhang J, Geng T, Liu Z, Xie X, Li Q (2021) Navigation performance analysis of LEO augmented BDS-3 navigation constellation. In: China Satellite Navigation Conference (CSNC) 2021 proceedings. Springer, Singapore, pp 521–530
41. Hu Z, Chen G, Zhang Q, Guo J, Su X, Li X, Zhao Q, Liu J (2013) An initial evaluation about BDS navigation message accuracy. In: China Satellite Navigation Conference (CSNC) 2013 proceedings. Springer, Berlin Heidelberg, pp 479–491